Electron tomography, three-dimensional Fourier analysis and colour prediction of a three-dimensional amorphous biophotonic nanostructure

Matthew D. Shawkey[1],*, Vinodkumar Saranathan[2], Hildur Pálsdóttir[3], John Crum[4], Mark H. Ellisman[4], Manfred Auer[3] and Richard O. Prum[2]

[1]*Department of Biology and Integrated Bioscience Program, University of Akron, Akron, OH 44325-3908, USA*
[2]*Department of Ecology and Evolutionary Biology, and Peabody Museum of Natural History, Yale University, New Haven, CT 06511, USA*
[3]*Life Sciences Division, Lawrence Berkeley National Laboratory, Mail Stop Donner, Berkeley, CA 94720, USA*
[4]*National Center for Microscopy and Imaging Research, University of California San Diego, La Jolla, CA 92093, USA*

Organismal colour can be created by selective absorption of light by pigments or light scattering by photonic nanostructures. Photonic nanostructures may vary in refractive index over one, two or three dimensions and may be periodic over large spatial scales or amorphous with short-range order. Theoretical optical analysis of three-dimensional amorphous nanostructures has been challenging because these structures are difficult to describe accurately from conventional two-dimensional electron microscopy alone. Intermediate voltage electron microscopy (IVEM) with tomographic reconstruction adds three-dimensional data by using a high-power electron beam to penetrate and image sections of material sufficiently thick to contain a significant portion of the structure. Here, we use IVEM tomography to characterize a non-iridescent, three-dimensional biophotonic nanostructure: the spongy medullary layer from eastern bluebird *Sialia sialis* feather barbs. Tomography and three-dimensional Fourier analysis reveal that it is an amorphous, interconnected bicontinuous matrix that is appropriately ordered at local spatial scales in all three dimensions to coherently scatter light. The predicted reflectance spectra from the three-dimensional Fourier analysis are more precise than those predicted by previous two-dimensional Fourier analysis of transmission electron microscopy sections. These results highlight the usefulness, and obstacles, of tomography in the description and analysis of three-dimensional photonic structures.

Keywords: biophotonics; structural colour; tomography; Fourier analysis; feathers

1. INTRODUCTION

Coloration of organisms is created by selective absorption of light by pigments, by coherent or incoherent scattering of light from structured or unstructured tissues or by combinations of these elements (Fox & Vevers 1960; Parker 2000; Hill & McGraw 2006). Structured bio-optical tissues can be classified as producing either iridescent (i.e. changing colour with angle of viewing or illumination; Newton 1704) or

*Author for correspondence (mshawkey@nature.berkeley.edu).

One contribution of 13 to a Theme Supplement 'Iridescence: more than meets the eye'.

non-iridescent colours (Parker 1998; Prum 2006). In feathers, iridescent colours are produced by ordered stacks of melanin granules in the β-keratin of feather barbules, while non-iridescent colours (figure 1a) are produced by 'spongy' amorphous arrays of air-filled voids in the β-keratin of medullary cells of feather barbs (reviewed in Prum 2006). Most structural colour-producing biological materials are photonic structures with spatial variation in refractive index (Vukusic & Sambles 2003). The heterogeneity in the refractive index of these structures allows some wavelengths of light to propagate through them, while others are selectively back-scattered (Joannopoulos *et al.* 2008), creating vivid observable colours.

Photonic structures may vary in refractive index over one, two or three dimensions. One-dimensional

biophotonic nanostructures include various thin films and multilayer reflectors (Land 1972; Parker *et al.* 1998). Two-dimensional structures include arrays of parallel collagen fibres in avian skin (Prum & Torres 2003*a*) and anti-reflective 'nipple arrays' in butterfly corneas (Stavenga *et al.* 2006). Three-dimensional photonic structures include opal analogues (Parker *et al.* 2003), inverse opal analogues (Morris 1975) and spongy medullary bird feathers (Prum 2006). In addition to the variation in the dimensionality of refractive index (Joannopoulos *et al.* 2008), photonic structures can also vary in the degree of periodicity or order in refractive index. In classical crystal-like nanostructures, the periodicity of variation in refractive index extends over large spatial scales (i.e. over many wavelengths). In amorphous or quasi-ordered nanostructures, there is only short-range order in the periodicity of refractive index limited to the local scale of the nearest-neighbour element or scatterer (Prum & Torres 2003*b*). Variation in both dimensionality and degree of periodicity contributes greatly to the overwhelming diversity of structural colour-producing biological nanostructures.

Describing and analysing the optical properties of three-dimensional amorphous nanostructures—such as the spongy medullary layer—has been particularly challenging. Recent studies using two-dimensional Fourier analysis of transmission electron microscopy (TEM) cross sections have demonstrated that these materials are highly ordered at small spatial scales (Prum *et al.* 1998, 1999, 2003). Optical predictions from these Fourier analyses have falsified the century-old hypothesis that these structures produce colour by incoherent or Rayleigh scattering (Prum *et al.* 1998). Although these analyses convincingly demonstrate that the spongy layer is responsible for a reflectance peak at a discrete wavelength, the peaks and shapes of the predicted reflectance spectra are subject to substantial errors (Prum *et al.* 1998, 2006; Shawkey *et al.* 2003, 2006). One explanation for this discrepancy is that two-dimensional Fourier analyses are not sufficient to describe accurately the periodicity of a three-dimensional nanostructure. This hypothesis is supported by the stronger congruence between measured and predicted reflectance spectra from two-dimensional Fourier analysis of quasi-ordered two-dimensional nanostructures in mammalian and avian skin (Prum & Torres 2003*a*, 2004).

Here, we combine tomographic reconstruction with intermediate voltage electron microscopy (IVEM) data for the first three-dimensional description of a biophotonic nanostructure of the spongy medullary barb keratin of the eastern bluebird (*Sialia sialis*). IVEM can handle much thicker samples (typically 250–300 nm) compared with traditional TEM (typically 70–90 nm). For tomographic reconstruction, images are taken at regular angular increments, and, upon three-dimensional reconstruction, nanostructural features can be observed by examining nanometre-thick digital slices through the sample (Frey *et al.* 2006). We used Fourier analysis of the full three-dimensional dataset to describe the nanoscale variation in composition across all dimensions within the nanostructure, and to
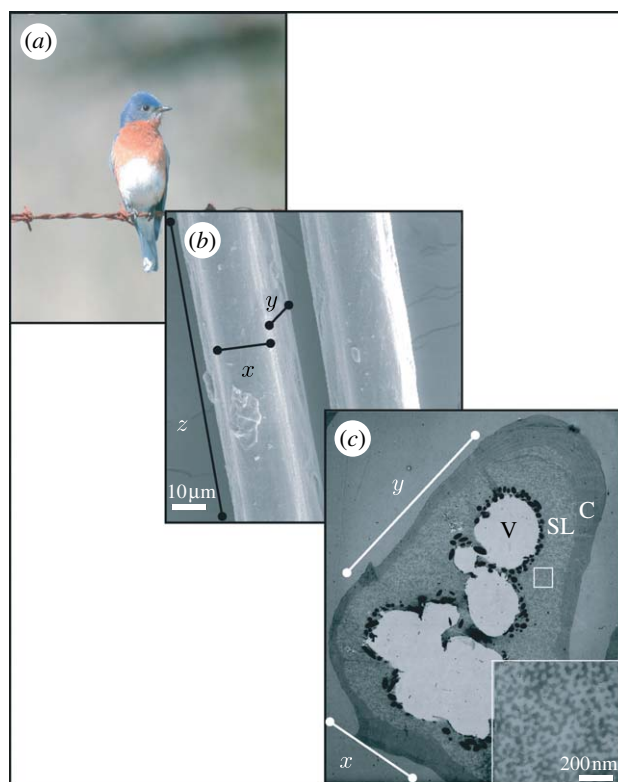

Figure 1. Anatomy of spongy medullary barb tissue. (*a*) Image of an eastern bluebird *S. sialis* (photo by Mark Liu) showing feathers with blue colour created by coherent scattering of light from spongy tissue in feather barbs. (*b*) SEM image of the outer surface of blue feather barbs illustrating the dimensions (*x,y,z*) examined in this paper. (*c*) Two-dimensional TEM image of a transverse section through a single feather barb. The *x* and *y* planes are illustrated. Moving inwards, the layers shown are the outer keratin cortex (C), spongy medullary layer (SL) and vacuole (V). Cell boundaries (dark lines) can be seen in the upper left section of the cross section. The square inset shows a close-up of the spongy layer.

predict its structural colour production based on Benedek's coherent scattering hypothesis (Benedek 1971; Prum 2006).

2. EXPERIMENTAL

2.1. Spectrometry

Rump feathers from one eastern bluebird were randomly chosen from a large collection in our laboratories. For colour analysis, we used the methods of Shawkey *et al.* (2003). Briefly, we taped feathers in stacks of five directly on top of one another to black construction paper, and recorded spectral data from five haphazardly chosen points on the blue portion of this stack using an Ocean Optics S2000 spectrometer (range 250–880 nm; Dunedin, FL) with a bifurcated micrometre fibre-optic probe held normal to and 5 mm from the feather surface using a probe holder (RPH-1; Ocean Optics). The reading area of 2 mm diameter of light was illuminated by both a UV (D-2000 deuterium bulb; Ocean Optics) and a visible (tungsten–halogen bulb) light source. All data were generated relative to a white standard (WS-1; Ocean Optics).

2.2. Electron tomography sample preparation

For a thorough review of electron tomographic principles and methodology, see Frey *et al.* (2006). Blue colour is localized in the distal sections of bluebird feather barbs; thus we cut coloured portions of feather barbs and dehydrated them by incubation in 100 per cent ethanol twice and 100 per cent propylene oxide once. We then infiltrated them with Epon 812 (Electron Microscopy Sciences, Hatfield, PA) in successive concentrations of 15, 50, 70 and 100 per cent. Each of these infiltration steps was performed under vacuum in a desiccator for 24–48 hours. We placed barbs into moulds, with the most distal tip of the barb at the top of the mould, cured the blocks in an oven at 68°C for 24 h and cut 80–1500 nm thick cross sections using a diamond knife (Diatome, Switzerland) on a Reichert (Buffalo, NY) ultramicrotome. We picked these sections up with clamshell grids (Ted Pella, Redding, CA) coated with formvar on one side, stained grids with uranyl acetate and Sato's (1968) lead citrate and coated them with carbon. For accurate alignment of two-dimensional projection images, 10–15 nm colloidal gold fiducials (BBI Research, Inc., Madison, WI) were applied as markers.

2.3. Electron tomography

We collected a dual-axis tilt series on an approximately 1200 nm thick section of spongy tissue from $-60°$ to $+60°$ at $2°$ increments on a JEOL 4000FX microscope at 400 kV at the National Center for Microscopy and Imaging Research at the University of California, San Diego. Thickness of the sample was chosen to maximize repetition of the periodic structure of our sample in the third dimension (estimated at approximately 100 nm based on calculations from two-dimensional samples) within the limits of IVEM electron-beam penetration. To limit data anisotropy, we performed a dual-axis reconstruction and collected data over the maximum range of adequate electron-beam penetration (Lucic *et al.* 2005; Frey *et al.* 2006). We reconstructed a three-dimensional tomogram using algorithms in the IMOD tomography package (Kremer *et al.* 1996) and viewed reconstructions using IMOD and University of California San Francisco (UCSF) Chimera (Pettersen *et al.* 2004).

These reconstructions are stacks of images with dimensions $x \times y \times 1$ voxel referred to as density maps. Each voxel in our density map represents 1 nm. Because Fourier analysis works more efficiently on cubes with dimensions of n^3, we chose two $1024 \, \text{nm}^3$ areas of pure spongy tissue from the centre of the thick sample for analysis. We sampled from the centre because this area was best defined and showed the fewest interpolation artefacts.

2.4. Definition of dimensions and planes for tomography

We defined x as the medial–lateral dimension, y as the dorsal–ventral (or obverse–reverse) dimension and z as the proximal–distal dimension (figure 1*b*). Thus, the thickness of the section corresponds to the z-dimension, along the length of the barb. The xy plane is the transverse cross-sectional plane of the barb (used in numerous other studies; figure 1*c*), while the xz and yz planes are visualized by rotating the structure $90°$ on the x- and y-axes, respectively.

2.5. Fourier analysis of the biophotonic nanostructure

We analysed images and density maps from the thick section using a modified version of Prum & Torres' (2003*b*) Fourier tool for biological nano-optics that was expanded to perform a three-dimensional Fourier analysis on IVEM data, rather than the two-dimensional Fourier analyses on TEM images for which it was originally programmed. This MATLAB-based code uses Fourier analysis to determine whether the nanostructure of photonic tissue is sufficiently organized at an appropriate scale to produce colour by coherent light scattering alone (Prum & Torres 2003*b*; Prum 2006).

Briefly, each two-dimensional slice of the three-dimensional tomogram is Fourier transformed using the matrix algebra program MATLAB's fast Fourier transform (*fft2*) algorithm. The zero-frequency Fourier components are shifted to the origin of these two-dimensional matrices and the results are stored in a three-dimensional stack. Subsequently, the matrix of two-dimensional transforms is Fourier transformed along the third dimension and the zero-frequency components are shifted to the origin. The square of the absolute value of the resulting matrix gives the three-dimensional Fourier power spectrum. This is equivalent to taking the three-dimensional Fourier transform of the entire three-dimensional tomogram at once, as a multidimensional Fourier transform is a separable operation over each dimension (Goodman 1996).

We used a refractive index of 1.54 for β-keratin (Brink & van der Berg 2004) and 1.0 for air in our estimation of the average refractive index of the spongy medullary barb nanostructure. The average refractive index (n_{avg}) of the spongy tissue is estimated by weighting the respective refractive indices of keratin and air with the relative frequency of the distribution of keratin (dark) and air (light) elements obtained from a two-partition histogram of the distribution of dark and light pixels over the entire tomogram (Prum & Torres 2003*b*). Specifically, each slice of the tomogram is first normalized, i.e. offset and scaled so that the minimum and maximum image value is between 0 and 1 (instead of 0 and 255). Pixels below the median image value and those above are set to 0 and 1, respectively, to binarize the image. The image is then locally median-filtered in a 2×2 pixel neighbourhood around each pixel in the input image using the *medfilt2* function to remove some amount of noise. We find that the 2×2 pixel neighbourhood is more optimal than the default 3×3 or larger neighbourhoods, as they tend to progressively discard data along with noise. A two-bin histogram of the binary image intensity is used to estimate the relative composition of keratin and air to arrive at n_{avg}. The array of n_{avg} values for all the slices is then averaged to arrive at the global value for the tomogram.

We obtained a value of 1.2143 for n_{avg}, which remained stable within a tolerance of 3 per cent when the median-filtering neighbourhood was varied. However, we obtained a physically implausible value of 1.0212 when we used the raw tomogram without any image processing.

Subsequent azimuthal analysis of the three-dimensional Fourier power spectrum incorporating the estimated average refractive index allows the user to obtain a predicted reflectance spectrum (Prum *et al.* 1998, 1999). Azimuthal average of the three-dimensional Fourier power spectrum is calculated by defining concentric spherical shells corresponding to either equally spaced wavelength intervals (e.g. 100 bins of 5 nm interval between 300 and 800 nm covering the entire visible spectrum) or inverse spatial frequency bins (between 0 and $0.02\,\mathrm{nm}^{-1}$ covering all optical phenomena; see Prum & Torres 2003b). Since the Fourier power distribution is essentially a volume (under the graph of the square of the Fourier transform), the three-dimensional azimuthal averages are multiplied by the square of the radii of the respective spherical bins to produce a quantity proportional to the volume of the spherical shell over each bin of frequencies. The azimuthally averaged power values are expressed in per cent visible Fourier power after normalizing by the total power across all inverse spatial frequencies corresponding to visible wavelengths. The predicted reflectance is then given by the relative distribution of the Fourier power expressed as normalized azimuthal averages over the wavelength bins (Benedek 1971). The predicted reflectance peak λ_{pk} follows from Bragg's law and is given by (Benedek 1971; Prum 2006)

$$\lambda_{pk} = 2 \times n_{avg} \times \frac{1}{k_{pk}},$$

where n_{avg} is the average refractive index and k_{pk} is the peak spatial frequency. For a more detailed description of the Fourier tool, see Prum & Torres (2003b). A GUI-based version of the three-dimensional tool will be made available in the public domain once a detailed description of the tool is published elsewhere.

2.6. Morphological analysis

For morphological analysis, we used either the raw data (thin section) or the data that had been binned (pixels averaged) four times to a final resolution of $4\,\mathrm{nm\ voxel}^{-1}$ (thick section). The periodicity of spongy layer (diameter of keratin rods and air spaces) is approximately 100 nm (Shawkey *et al.* 2003, 2005), and thus high resolution was not needed and made density maps unnecessarily bulky. Using the slicer module in IMOD, we examined tissue morphology by inspecting the density map slice by slice, in orthogonal and non-orthogonal arbitrary orientations. Using Chimera, we surface rendered median- or bilateral-filtered (Jiang *et al.* 2003) portions of the three-dimensional volume to explore the density in three dimensions and to ensure that no patterns emerged which may have been missed by slice-by-slice inspection.

2.7. Scanning electron microscopy

To cross-validate our electron tomographic three-dimensional morphological data, we examined the spongy layer on a scanning electron microscope (SEM, Hitachi S-5000) at the electron microscope laboratory at the University of California, Berkeley. To cut longitudinal sections, we used epoxy to mount barbs lengthwise to pieces of carbon tape attached to the blunt end of blank Epon TEM blocks. We then cut through the barb longitudinally using a diamond knife on a microtome. The barbs were then placed on stubs and sputter-coated with gold before viewing in the SEM.

3. RESULTS

Spongy medullary keratin cells sit beneath a cortex of solid keratin, and above a layer of melanin granules surrounding hollow central vacuoles (figure 1c). The three-dimensional dataset was acquired from the spongy keratin matrix within single medullary cells (square inset, figure 1c). The final dimensions of our thick section map were $4004 \times 4087 \times 1224$ nm.

The density map from the thick section revealed the larger scale ordering of the spongy tissue. The sequence of *xy* images in the three-dimensional dataset demonstrates that the colour-producing nanostructure of eastern bluebirds is an irregular, completely interconnected (i.e. bicontinuous; Shimizu *et al.* 2004) network of keratin rods and air voids forming a characteristic 'channel'-type structure (figure 2; see movies 1–3 in the electronic supplementary material). The keratin forms interconnected, anastomosing, net-like layers with equivalently shaped air channels. Slices through the *z*-axis show random orientation of keratin rods on the *xy* plane (figure 2b; see movie 1 in the electronic supplementary material). Owing to the limited tilt range data and the resulting error, features along the *z*-axis are distorted, elongated and are less well resolved (figure 2c,d; see movies 2 and 3 in the electronic supplementary material). This elongation is particularly noticeable on the *xz* plane (figure 2c; see movie 2 in the electronic supplementary material).

The three-dimensional Fourier power spectra of the cubic datasets feature a nearly spherical shell at intermediate spatial frequencies in most directions (figure 3a,b). The spherical shape is distorted along the *z*-axis by depressions, or 'dimples', of low spatial frequency (figure 3a). The sphere in the three-dimensional transform is not completely hollow, but shows some low spatial frequency features because of the distortion along the *z*-dimension (see movies 4–7 in the electronic supplementary material). We also examined the average power spectra along the *x*-, *y*- or *z*-axes individually (figure 3c–e). These are equivalent to taking the average of the stack of two-dimensional Fourier power spectra along each of the three dimensions. The resulting two-dimensional average Fourier power spectrum along the *z*-axis, where the distortion in the *z*-dimension is best controlled, shows a discrete ring of high power at intermediate spatial frequency (figure 3e), indicating local nanoscale order that is equivalent along multiple directions within the
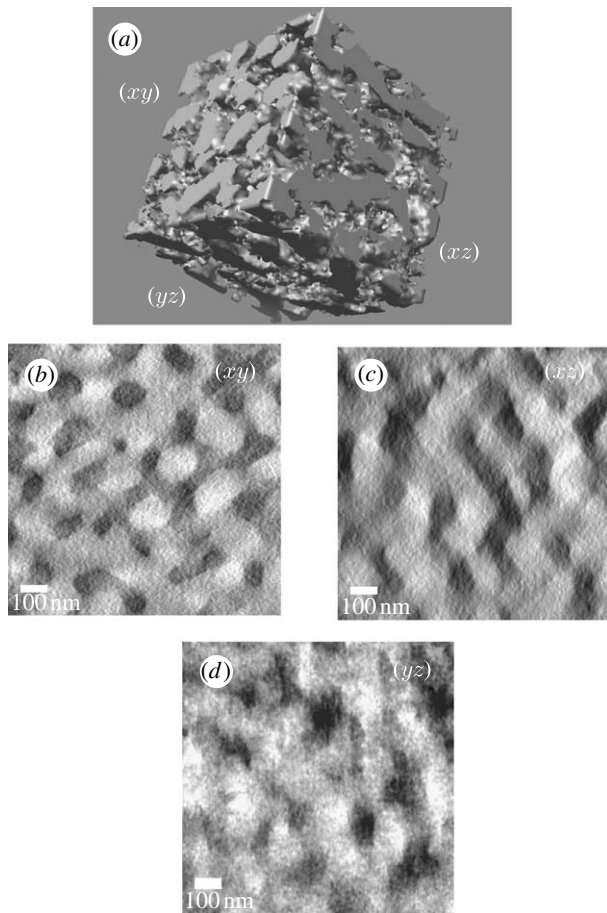
Figure 2. Three-dimensional morphology from tomographic reconstructions of colour-producing spongy tissue from eastern bluebird *S. sialis* feathers. (*a*) Three-dimensional surface rendering of a 1024 nm³ section of spongy tissue. (*b–d*) The two-dimensional planes from the tomographic reconstruction. The dark material represents keratin and the light material is air. Surface rendering was performed using UCSF Chimera, while the individual planes are from reconstructions computed using IMOD. Elongation and blurring of features in the *xz* and *yz* planes are caused by tomographic error.

xy plane. The two-dimensional average power spectrum in the *x*- and *y*-axes has a variable 'bow-tie' shape (figure 3*c,d*), showing the low-frequency distortion in the *z*-axis above and below the origin which eliminates the spherical shape from these perspectives.

Both the peaks and the shapes of the predicted reflectance spectra based on the azimuthal average of the three-dimensional Fourier power spectra match the measured reflectance spectra quite well (figure 4). This indicates that the nanostructure is sufficiently periodic at the appropriate spatial scale in all three dimensions to produce the observed reflectance by coherent scattering. SEM images further support that the elongated appearance of keratin rods in spongy layer along the *z*-direction is a consequence of tomographic error and do not represent real differences.

We took SEM images along the *xz* plane for a comparison with surface renderings from tomography (figure 5). Keratin rods in the surface renderings appear elongated in the *z*-direction compared with those in the SEM image (figure 5). The stretched appearance of features in tomograms in the *z*-direction is a common

and well-known error in tomography resulting from the fact that the limited electron penetration of an unusually thick specimen only allowed data collection of 120°, resulting in a missing pyramid of information and hence in data anisotropy along the *z*-dimension (Lucic *et al.* 2005; Frey *et al.* 2006). The fact that the distortion in the data occurs precisely in the *z*-dimension indicates that it is an artefact of the tomography and not a feature of the tissue, because there is no biological reason for this distortion in precisely that direction. Furthermore, SEM images taken along the *xz* plane from a section of the spongy medullary keratin show no distortion in the *z*-dimension. However, from the data presented, it is clear that electron tomography may be used to address the question of nanoscale three-dimensional architecture, as it allows the calculation of a three-dimensional Fourier transform, which is not obtainable from SEM or conventional TEM images. SEM nicely complements the results, and we therefore suggest that future studies should contain both approaches.

4. DISCUSSION

These tomographic data provide the first three-dimensional visualization of a colour-producing three-dimensional amorphous nanostructure. Argyros *et al.* (2002) obtained electron tomography data from a crystal-like photonic butterfly scale, but, because their dataset was limited to less than twice the periodicity of the structure in the *z*-dimension (500 versus 300 nm), they could not examine three-dimensional periodicity directly. Previous two-dimensional Fourier predictions of the hue values for spongy medullary keratin have not been very accurate, deviating from measured values by as much as 70 nm (Prum *et al.* 1998*b*, 1999; Shawkey *et al.* 2003). Furthermore, shapes of predicted spectra rarely match measured curves (Doucet *et al.* 2004; Shawkey *et al.* 2006). The substantially higher accuracy of colour predictions based on these three-dimensional tomography data indicates that a complete three-dimensional description of the nanostructure is extremely useful in understanding and modelling structural colour production, particularly for amorphous photonic structures. However, certain limitations in tomographic data collection must be considered in subsequent analysis.

The three-dimensional Fourier analysis indicated that the pattern of medullary keratin analysed differed in ultrastructure in the *z*-dimension, compared with the *xy* plane. However, comparisons of SEM images with tomographic reconstructions show that variation in the *z*-dimension is not characteristic of spongy keratin, and is caused by tomographic error. While we collected and combined data along two perpendicular tilt axes, each dataset was only recorded over 120°, hence resulting in significant data anisotropy (Lucic *et al.* 2005; Frey *et al.* 2006). The limitation in our data collection geometry is a direct result of the thickness of our specimen and the limited penetration depth of the electron beam at angles higher than ±60°. However, thick sections were key to our study as we aimed to have
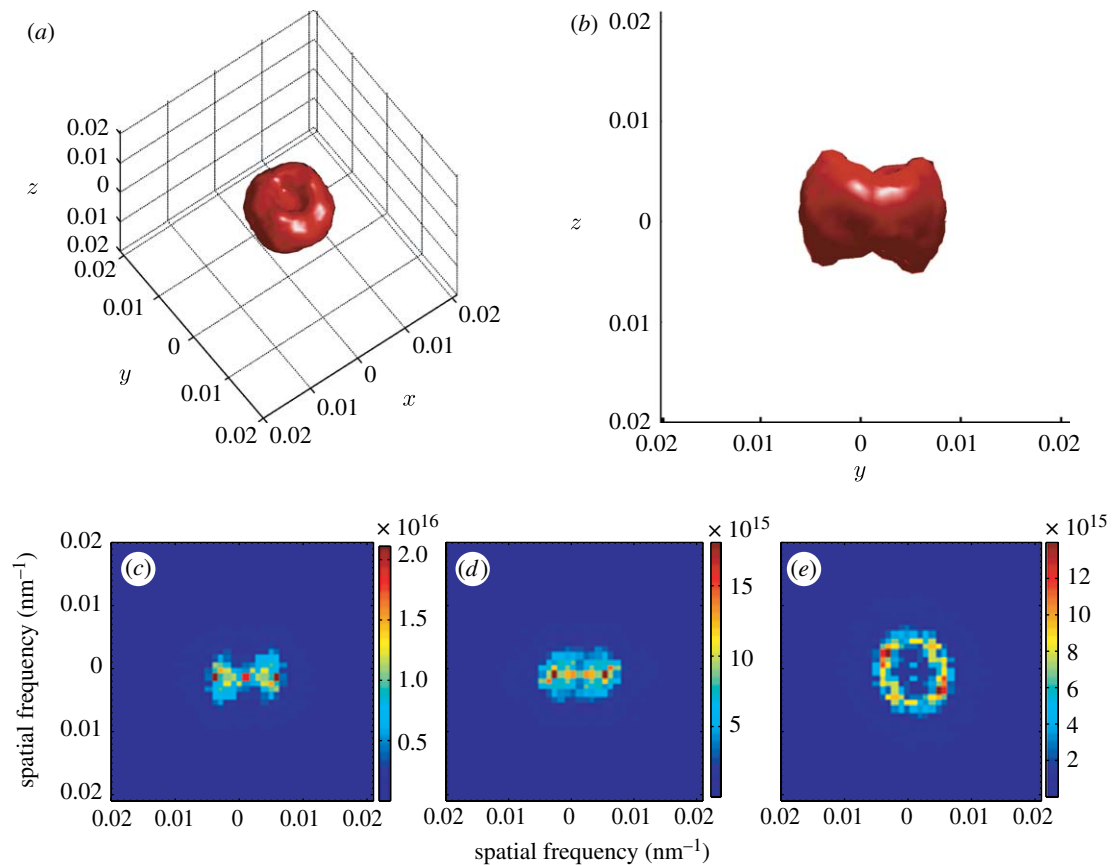
Figure 3. Fourier power spectra from tomographic reconstructions of colour-producing spongy tissue from eastern bluebird (*S. sialis*) feathers. (*a,b*) Three-dimensional Fourier power spectrum of a 1024 nm³ tomographic section of spongy tissue shown (*a*) tilted and in (*b*) lateral view. This rendering of the three-dimensional Fourier transform depicts the outer surface of the Fourier transform distribution obtained by coding Fourier power values above a certain threshold to red. (*c–e*) Averaged projections of the three-dimensional Fourier power spectra along different axes: (*c*) *x*-axis, (*d*) *y*-axis and (*e*) *z*-axis. The ring shape of the three-dimensional power spectrum indicates quasi-periodic order that is equivalent over much of the nanostructure, while polar dimples along the *z*-axis are caused by the elongation of features in the *z*-dimension caused by tomographic error.
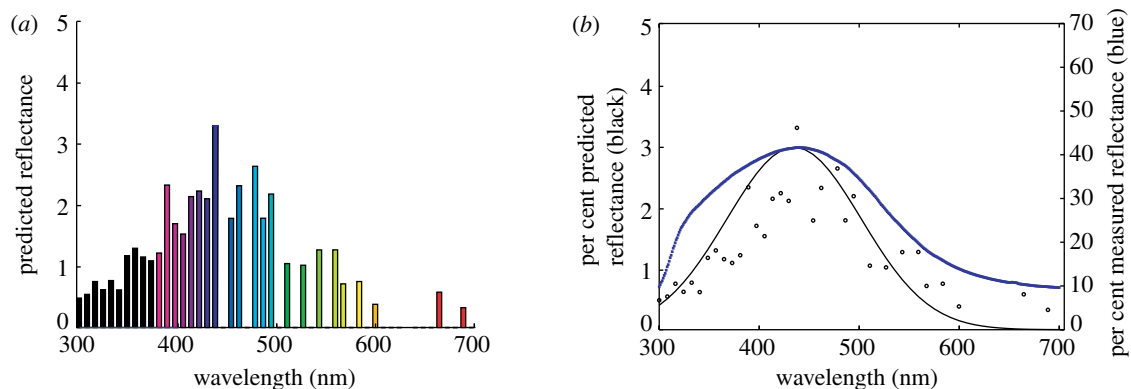

Figure 4. (*a*) Predicted reflectance spectra (colour bars) from spongy tissue of eastern bluebird (*S. sialis*) feathers. (*b*) Measured (blue) and predicted (black circles with Gaussian fit) reflectance spectra from spongy tissue of eastern bluebird (*S. sialis*) feathers. The reflectance prediction is in per cent visible Fourier power and is based on an azimuthal average analysis of the three-dimensional Fourier power spectrum data performed by defining concentric spherical shells corresponding to equally spaced wavelength intervals. Some bins, especially the higher wavelength ones (particularly visible in (*a*)), contain no Fourier power owing to 'leakage' as their power overlaps with neighbouring bins creating a jagged reflectance profile (Briggs & Henson 1995).

sufficient repeating units in the *z*-dimension to render Fourier analysis meaningful. In any case, the predicted reflectance at normal incidence appears to have only been minimally affected. New advances in tomography, such as rotation holders that allow 180° data collection

(M. H. Ellisman 2008, unpublished data), may improve isotropy in the future, but these results already illustrate the power of electron tomography. As always, it is important to validate tomographic data with at least one other independent method.
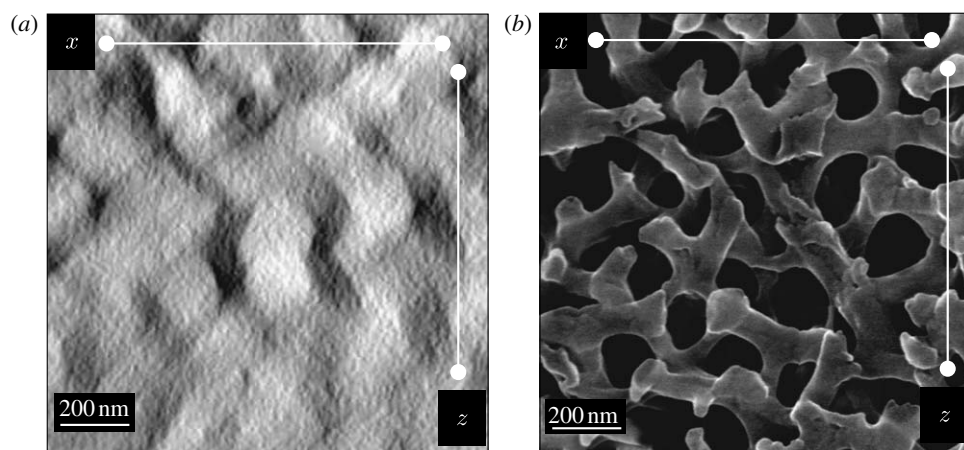
Figure 5. (*a*) Tomographic reconstruction and (*b*) SEM image of the *xz* plane from the spongy layer of an eastern bluebird (*S. sialis*) feather. Note quasi-ordered orientation of the air voids (light in (*a*) and dark in (*b*)) and keratin in the SEM when compared with the rather columnar orientation of the keratin channels and air voids in the tomographic reconstruction.

Both tomographic and SEM data show that the channel-type nanostructure of the eastern bluebird is bicontinuous—i.e. all keratin channels and all air voids are interconnected with one another, respectively. This connection and their overall amorphous organization support the proposal that they are formed through a process of self-assembly similar to that observed in block copolymers (Dyck 1971; Prum 2006). Some of these polymers self-assemble into amorphous, bicontinuous structures that bear striking resemblances to spongy tissue (Shimizu *et al.* 2004). Many three-dimensional photonic structures in invertebrates also appear to be bicontinuous (Vukusic & Sambles 2003), and tomography data will allow us to verify this and even compare their structures and, potentially, development with those in birds (Shawkey *et al.* 2009).

Our results show that IVEM tomography is a useful technique for resolving the structure of three-dimensional biological nanostructures, but not surprisingly needs to be used carefully. Every possible measure should be taken to minimize tomographic error, and results should ideally be compared with those from at least one other technique, such as SEM. The application of tomography to study biophotonic structures is likely to increase in the future, as it is one of the few available methods for collecting data that can be visualized and analysed in three dimensions. SEM is useful for examining the surface features of tissues, but SEM data are still only a two-dimensional representation of an object and thus cannot be used in three-dimensional analyses such as those presented here. Ultrathin serial section reconstruction (Ware & Lopresti 1975) has been applied to numerous tissue types ranging from dendritic spines (Harris 1999) to an entire animal, the nematode *Caenorhabditis elegans* (White *et al.* 1986). However, such techniques are not practical when the thickness of the sections is similar to the nanoscale periodic structures being resolved (Oppenheim *et al.* 1997; M. D. Shawkey, unpublished data). An interesting approach for future studies may be dual-beam focused ion beam/SEM, which avoids some of the caveats of electron tomography and may be particularly useful for samples where a resolution of

5–20 nm is sufficient. Finally, we have shown that some of the errors associated with two-dimensional Fourier analysis can be alleviated by the use of three-dimensional methods, and therefore encourage their future use. Moving the study of three-dimensional biophotonic structures into the third dimension will considerably advance our understanding of their optics, development and evolution.

REFERENCES

Argyros, A., Manos, S., Large, M. C. J., McKenzie, D. R., Cox, G. C. & Dwarte, D. M. 2002 Electron tomography and computer visualization of a three-dimensional 'photonic' crystal in a butterfly wing-scale. *Micron* **33**, 483–487. (doi:10.1016/S0968-4328(01)00044-0)

Benedek, G. B. 1971 Theory of transparency of the eye. *Appl. Optics* **10**, 459–473. (doi:10.1364/AO.10.000459)

Brink, D. J. & van der Berg, N. G. 2004 Structural colours from the feathers of the bird *Bostrychia hagedash*. *J. Phys. D: Appl. Phys.* **37**, 813–818. (doi:10.1088/0022-3727/37/5/025)

Briggs, W. L. & Henson, V. E. 1995 *The DFT*. Philadelphia, PA: Society for Industrial and Applied Mathematics.

Doucet, S. M., Shawkey, M. D., Rathburn, M. D., Mays Jr, H. L. & Montgomerie, R. 2004 Concordant evolution of plumage colour, feather microstructure, and a melanocortin receptor gene between mainland and island populations of a fairy-wren. *Proc. R. Soc. B* **271**, 1663–1670. (doi:10.1098/rspb.2004.2779)

Dyck, J. 1971 Structure and colour-production of the blue barbs of *Agapornis roseicollis* and *Cotinga maynana*. *Z. Zellforsch.* **115**, 17–29. (doi:10.1007/BF00330211)

Fox, H. M. & Vevers, G. 1960 *The nature of animal colors.* New York, NY: Macmillan.

Frey, T. G., Perkins, G. A. & Ellisman, M. H. 2006 Electron tomography of membrane-bound cellular organelles. *Annu. Rev. Biophys. Biomol. Struct.* **35**, 199–224. (doi:10.1146/annurev.biophys.35.040405.102039)

Goodman, J. W. 1996 *Introduction to Fourier optics.* New York, NY: McGraw-Hill.

Harris, K. M. 1999 Structure, development, and plasticity of dendritic spines. *Curr. Opin. Neurobiol.* **9**, 343–348. (doi:10.1016/S0959-4388(99)80050-6)

Hill, G. E. & McGraw, K. J. (eds) 2006 *Bird coloration. Mechanisms and measurements*, vol. I. Boston, MA: Harvard University Press.

Jiang, W., Baker, M. L., Wu, Q., Bajaj, C. & Chiu, W. 2003 Applications of a bilateral denoising filter in biological electron microscopy. *J. Struct. Biol.* **144**, 114–122. (doi:10.1016/j.jsb.2003.09.028)

Joannopoulos, J. D., Johnson, S. G., Winn, J. N. & Meade, R. D. 2008 *Photonic crystals: molding the flow of light.* Princeton, NJ: Princeton University Press.

Kremer, J. R., Mastronarde, D. N. & McIntosh, J. R. 1996 Computer visualization of three-dimensional image data using IMOD. *J. Struct. Biol.* **116**, 71–76. (doi:10.1006/jsbi.1996.0013)

Land, M. F. 1972 The physics and biology of animal reflectors. *Prog. Biophys. Mol. Biol.* **24**, 77–106. (doi:10.1016/0079-6107(72)90004-1)

Lucic, V., Forster, F. & Baumeister, W. 2005 Structural studies by electron tomography: from cells to molecules. *Ann. Rev. Biochem.* **74**, 833–865. (doi:10.1146/annurev.biochem.73.011303.074112)

Morris, R. B. 1975 Iridescence from diffraction structures in the wing scales of *Callophys rubi*, the green-haired streak. *Proc. R. Soc. Ent. A* **59**, 149–154.

Newton, I. 1704 *Opticks.* Mineola, NY: Dover Publications.

Oppenheim, A. V., Willsky, A. S. & Nawab, S. H. 1997 *Signals and systems.* Upper Saddle River, NJ: Prentice-Hall.

Parker, A. R. 1998 The diversity and implications of animal structural colors. *J. Exp. Biol.* **201**, 2343–2347.

Parker, A. R. 2000 515 Million years of structural colour. *J. Opt. A- Pure Appl. Opt.* **2**, R15–R28. (doi:10.1088/1464-4258/2/6/201)

Parker, A. R., McKenzie, D. R. & Large, M. C. J. 1998 Multilayer reflectors in animals using green and gold beetles as contrasting examples. *J. Exp. Biol.* **201**, 1307–1313.

Parker, A. R., Welch, V. L., Driver, D. & Martini, N. 2003 Structural colour: opal analogue discovered in a weevil. *Nature* **426**, 786–787. (doi:10.1038/426786a)

Pettersen, E. F., Goddard, T. D., Huang, C. C., Couch, G. S., Greenblatt, D. M., Meng, E. C. & Ferrin, T. E. 2004 UCSF Chimera: a visualization system for exploratory research and analysis. *J. Comput. Chem.* **25**, 1605–1612. (doi:10.1002/jcc.20084)

Prum, R. O. 2006 Anatomy, physics and evolution of avian structural colors. In Bird coloration: mechanisms, vol. I (eds G. E. Hill & K. J. McGraw). Mechanisms and measurements. Boston, MA: Harvard University Press.

Prum, R. O. & Torres, R. 2003a Structural colouration of avian skin: convergent evolution of coherently scattering dermal collagen arrays. *J. Exp. Biol.* **206**, 2409–2429. (doi:10.1242/jeb.00431)

Prum, R. O. & Torres, R. H. 2003b A Fourier tool for the analysis of coherent light scattering by bio-optical nanostructures. *Integr. Comp. Biol.* **43**, 591–602. (doi:10.1093/icb/43.4.591)

Prum, R. O. & Torres, R. H. 2004 Structural colouration of mammalian skin: convergent evolution of coherently scattering dermal collagen arrays. *J. Exp. Biol.* **207**, 2157–2172. (doi:10.1242/jeb.00989)

Prum, R. O., Torres, R., Williamson, S. & Dyck, J. 1998 Constructive interference of light by blue feather barbs. *Nature* **396**, 28–29. (doi:10.1038/23838)

Prum, R. O., Torres, R., Williamson, S. & Dyck, J. 1999 Two-dimensional Fourier analysis of the spongy medullary keratin of structurally coloured feather barbs. *Proc. R. Soc. B* **266**, 13–22. (doi:10.1098/rspb.1999.0598)

Prum, R. O., Andersson, S. & Torres, R. H. 2003 Coherent scattering of ultraviolet light by avian feather barbs. *Auk* **120**, 163–170. (doi:10.1642/0004-8038(2003)120[0163:CSOULB]2.0.CO;2)

Prum, R. O., Quinn, T. & Torres, R. H. 2006 Anatomically diverse butterfly scales all produce structural colours by coherent scattering. *J. Exp. Biol.* **209**, 748–765. (doi:10.1242/jeb.02051)

Sato, T. 1968 A modified method for lead staining of thin sections. *J. Electron Microsc.* **17**, 158–159.

Shawkey, M. D., Estes, A. M., Siefferman, L. M. & Hill, G. E. 2003 Nanostructure predicts intraspecific variation in ultraviolet–blue plumage colours. *Proc. R. Soc. B* **270**, 1455–1460. (doi:10.1098/rspb.2003.2390)

Shawkey, M. D., Estes, A. M., Siefferman, L. & Hill, G. E. 2005 The anatomical basis of sexual dichromatism in non-iridescent, ultraviolet–blue structural coloration of feathers. *Biol. J. Linn. Soc.* **84**, 259–271. (doi:10.1111/j.1095-8312.2005.00428.x)

Shawkey, M. D., Balenger, S. L., Hill, G. E. & Siefferman, L. 2006 Mechanisms of evolutionary change in structural plumage coloration among bluebirds. *J. R. Soc. Interface* **3**, 527–532. (doi:10.1098/rsif.2006.0111)

Shawkey, M. D., Morehouse, N. I. & Vukusic, P. 2009 A protean palette: colour materials and mixing in birds and butterflies. *J. R. Soc. Interface* **6**, S221–S231. (doi:10.1098/rsif.2008.0459.focus)

Shimizu, K., Wang, H., Wang, Z., Matsuba, G., Kim, G. & Han, C. C. 2004 Crystallization and phase separation kinetics in blends of linear low-density polyethylene copolymers. *Polymer* **45**, 7061–7069. (doi:10.1016/j.polymer.2004.08.038)

Stavenga, D. G., Folleta, S., Palasantzas, G. & Arikawa, K. 2006 Light on the moth-eye corneal nipple array of butterflies. *Proc. R. Soc. B* **273**, 661–667. (doi:10.1098/rspb.2005.3369)

Vukusic, P. & Sambles, J. R. 2003 Photonic structures in biology. *Nature* **424**, 852–855. (doi:10.1038/nature01941)

Ware, R. W. & Lopresti, V. 1975 Three-dimensional reconstruction from serial sections. *Int. Rev. Cytol.* **40**, 325–440. (doi:10.1016/S0074-7696(08)60956-0)

White, J. G., Southgate, E., Thomson, J. N. & Brenner, S. 1986 The structure of the nervous system of the nematode *Caenorhabditis elegans*. *Phil. Trans. R. Soc. B* **314**, 1–340. (doi:10.1098/rstb.1986.0056)